


Long-period ordering induced by hydrogen doping in NdNiO₃ films on SrTiO₃ (001) substrates

Tomoki Deguchi ^{1,*}, Takeshi Hara ¹, Yuta Ishii², Hao-Bo Li ³, Azusa N. Hattori ³, Hidekazu Tanaka ³,
Hajime Sagayama^{4,†} and Yusuke Wakabayashi ^{1,‡}

¹Department of Physics, Graduate School of Science, *Tohoku University*, Sendai 980-8578, Japan

²Center for Basic Research on Materials (CBRM), *National Institute for Materials Science (NIMS)*,
1-2-1 Sengen, Tsukuba, Ibaraki 305-0047, Japan

³SANKEN (Institute of Scientific and Industrial Research), *The University of Osaka*, 8-1 Mihogaoka, Ibaraki, Osaka 567-0047, Japan

⁴Institute of Materials Structure Science, *High Energy Accelerator Research Organization*, Tsukuba, Ibaraki 305-0801, Japan



(Received 21 November 2025; revised 6 March 2026; accepted 31 March 2026; published 18 May 2026)

Hydrogen doping offers a versatile method to dynamically control the doping level of metal oxides over a wide range, yet it introduces strong lattice modulation whose structural details have been poorly investigated. Here, we elucidate the hydrogen-induced structural modulation in NdNiO₃ thin films using synchrotron x-ray diffraction. While the strain relaxed pristine film exhibits a bulklike $\sqrt{2} \times \sqrt{2} \times 2$ structure, the hydrogen-induced insulating phase adopts a $1 \times 1 \times 2$ structure with some incommensurate modulation. Our results provide the first direct experimental evidence for hydrogen-induced formation of a superstructure in rare-earth nickelates.

DOI: [10.1103/gd7h-6967](https://doi.org/10.1103/gd7h-6967)

I. INTRODUCTION

Carrier doping is a fundamental strategy to control the electronic properties of transition metal oxides. In perovskite oxides, A-site substitution has been widely employed to tune the 3d electron number and associated physical properties such as magnetism and transport. While this approach provides precise control of the nominal doping level over a wide range, it fixes the carrier concentration during synthesis. Reversible external control has been pursued through various approaches, including electric field gating via electric double layers [1–4] and chemical insertion of mobile ionic species [5–7]. Among chemical insertion methods, hydrogen insertion into transition metal oxides has emerged as a powerful route to induce large changes in electronic properties [8–11].

Rare-earth nickelates RNiO₃ provide a prototypical platform for studying correlation-driven metal-insulator transitions (MIT) [12]. These compounds exhibit a systematic evolution of the MIT temperature with rare-earth ionic radius, reflecting the interplay between bandwidth, electron correlation, and structural distortions [12]. The low-temperature insulating phase is accompanied by charge disproportionation and antiferromagnetic ordering [13–15], while the high-temperature metallic phase shows paramagnetic behavior.

Hydrogen insertion into RNiO₃ thin films induces a MIT with resistivity changes exceeding six orders of magnitude [5,11,16,17]. This process is reversible upon annealing, enabling potential applications in resistive switching and memristive devices [18–21]. Experimentally, hydrogen is typically introduced by exposing RNiO₃ films patterned with platinum catalysts to H₂ gas at elevated temperatures [5,22–27]. Hydrogen dissociates on the platinum surface and diffuses into the film over length scales of tens of micrometers within minutes.

Despite extensive investigations [5,6,16,22–25,27–32], the microscopic mechanism underlying the hydrogen-induced MIT remains incompletely understood. Key open questions include: which crystallographic sites does hydrogen occupy [6,30], what is the hydrogen stoichiometry in the insulating phase [23,25], and how does hydrogen insertion modify the crystal structure and electronic configuration. Addressing these questions requires direct structural characterization of hydrogenated RNiO₃ at the atomic scale.

Recent density functional theory (DFT) calculations [30] have provided theoretical insight into possible hydrogen configurations in H_x-RNiO₃, where x denotes the hydrogen concentration. Systematic studies for $R = \text{Sm}$, assuming a $2\sqrt{2} \times \sqrt{2} \times 2$ supercell, evaluated the energetic stability of various hydrogen arrangements after full structural optimization. Configurations with $x = 1$ and $x = 0.5$ were found to exhibit significantly lower total energies compared to other stoichiometries. Notably, the calculation for $x = 0.5$ configuration exhibits a layered arrangement of Ni valences, distinct from the checkerboard pattern [13–15,33,34] observed in the low-temperature insulating phase of bulk RNiO₃. However, experimental verification of these predicted structures has been lacking. Even whether hydrogen incorporation induces long-range structural ordering or forms a disordered solid solution remains an open question.

*Contact author: deguchi.tomoki.q6@dc.tohoku.ac.jp

†Present address: Nagoya University Synchrotron Radiation Research Center (NUSR), Nagoya University, Nagoya 464-8603, Japan.

‡Contact author: wakabayashi@tohoku.ac.jp

Here we address this issue through synchrotron x-ray diffraction studies of epitaxial NdNiO₃ thin films grown on SrTiO₃ (001) substrates. We compare the diffraction patterns of pristine and hydrogenated films. Our measurements reveal that hydrogen insertion drives the formation of a distinct crystallographic phase, absent in the pristine films, characterized by the wave vector $\frac{1}{2}\mathbf{c}_{\text{pc}}^*$ with incommensurate modulation, where the subscript pc denotes pseudocubic notation, while the alternating tilting of NiO₆ octahedra is substantially reduced. These results provide direct experimental evidence for the formation of layered structure in H_x-RNiO₃ and establish a structural framework for understanding the hydrogen-induced metal-insulator transition.

II. EXPERIMENT

Epitaxial NdNiO₃ thin films were grown on 10×10×0.5 mm³ SrTiO₃(100) substrates (Crystalbase Co.) using a pulsed laser deposition system with a handmade ceramic target under optimized growth conditions of 660 °C and oxygen pressure of 30 Pa. The laser energy (ArF, $\lambda = 193$ nm) was kept at 1.9 J/cm² with a repetition rate of 6 Hz. After deposition, the samples were cooled to room temperature with growth pressure in 30 minutes.

The surface of the NdNiO₃ films was covered with a Pt mesh catalyst to dissociate H₂ into atomic hydrogen. The Pt mesh had a pitch of 5 μm , similar to that used in Ref. [24]. A sample was split into two pieces. One piece was hydrogenated by annealing in Ar(96%)-H₂(4%) at 300 °C for 20 minutes (hereafter referred to as H-NNO), while the other piece was kept as a pristine reference (hereafter referred to as PR-NNO).

The lattice parameters of bulk NdNiO₃ in the *Pbnm* setting are $a_o = 5.389$ Å, $b_o = 5.382$ Å, and $c_o = 7.610$ Å [35], corresponding to a pseudocubic lattice parameter $a_{\text{pc}} = 3.807$ Å. Throughout this paper, we use the pseudocubic notation for indexing.

Synchrotron x-ray diffraction experiments were performed at a photon energy of 16 keV at beamlines BL-4C and BL-8B of the Photon Factory, KEK, Japan. At BL-8B, reciprocal space maps were obtained using the oscillation photograph method with a 2D detector (PILATUS3 S 1M) in air at room temperature. At BL-4C, Bragg reflection intensities were measured by the ω -scan method in vacuum at room temperature.

III. RESULTS AND ANALYSIS

First, we examined the structure of the PR-NNO film. Figures 1(a) and 1(b) show the reciprocal space maps of PR-NNO on the (*hk*1) and (*hk* $\frac{3}{2}$) planes, respectively. The in-plane lattice parameters are fully relaxed from those of the substrate. Although the centers of the substrate Bragg reflections are slightly offset from the $l = 1$ plane, tails of the strong substrate reflections are visible as sharp features in panel (a) [for example, those at (3,3) and (1,3) are prominent].

In addition to the film Bragg reflections at integer h , k , and l positions, many weak Bragg reflections appear at half-integer positions. The peak positions are consistent with the *Pbnm* unit cell of NdNiO₃ assuming all six possible multidomain variants (c_o oriented along the a_{pc} , b_{pc} , or c_{pc} directions, each

TABLE I. Structural parameters of the PR-NNO film. The lattice parameters are $a_{\text{pc}} = b_{\text{pc}} = 3.813$ Å, and $c_{\text{pc}} = 3.812$ Å. The corresponding parameters for the bulk structure [35] are also provided for comparison.

Par.	PR-NNO	Bulk
$x(\text{Nd})$	0.4836(5)	0.4799(6)
$y(\text{Nd})$	0.5131(6)	0.5142(6)
$x(\text{O1})$	0.226(5)	0.2190(7)
$y(\text{O1})$	0.218(6)	0.2111(7)
$x(\text{O2})$	0.500(7)	0.5004(4)
$y(\text{O2})$	0.287(5)	0.2846(4)
$z(\text{O2})$	0.285(10)	0.2878(4)
$U(\text{Nd})(\text{\AA}^2)$	0.0275(9)	0.0077(4)
$U(\text{Ni})(\text{\AA}^2)$	0.02	0.00646(13)
$U(\text{O1})(\text{\AA}^2)$	0.035(10)	0.0096(6)
$U(\text{O2})(\text{\AA}^2)$	$U(\text{O1})$	0.0111(5)

with either right- or left-handed coordination). Due to the multidomain structure and relaxed lattice parameters, the film Bragg reflections are broader than those of the substrate. The pseudocubic lattice parameters of PR-NNO are $a_{\text{pc}} = b_{\text{pc}} = 3.813$ Å and $c_{\text{pc}} = 3.812$ Å. Diffuse streaks extending from the strong film Bragg reflections (positions where $h + k + l$ is even) are attributable to dislocations parallel to the a_{pc} or b_{pc} axes [36]. This feature was observed only in some samples, suggesting that these diffuse streaks are not essential to the main functionality of NdNiO₃ films.

Given this information, we measured film Bragg reflection intensities using a large four-circle diffractometer to collect precise intensities under controlled illumination conditions [37]. Assuming the space group of PR-NNO is the same as that of the bulk, *Pbnm*, structural parameters were derived by Bayesian analysis [38,39]. The total number of Bragg reflections used for the refinement was 114, and the total number of structural parameters was 11. To reduce the number of structural parameters, we employed isotropic atomic displacement parameters U and used a common U for the two oxygen sites.

Figure 2 shows the observed Bragg intensities (I_{obs}) plotted against the calculated intensities (I_{calc}). The number of reflections with very strong intensities is limited due to overlap between intense substrate Bragg reflections and film reflections. This reduction in the number of accessible reflections limits information on the Ni site, which contributes Bragg intensity only at integer h , k , and l positions in the pseudocubic indexing. For this reason, we fixed $U(\text{Ni})$ at 0.02 Å². The Bayesian analysis yielded the structural parameters summarized in Table I, with an R value ($R = \frac{\sum |\sqrt{I_{\text{obs}}} - \sqrt{I_{\text{calc}}}|}{\sum \sqrt{I_{\text{obs}}}}$) of 0.106. The bulk values reported in Ref. [35] are also listed for comparison. The obtained atomic positions for PR-NNO are close to those of bulk NdNiO₃.

Figures 1(c) and 1(d) show the reciprocal space maps of H-NNO. Clear changes in the intensity distribution caused by hydrogen doping indicate a substantial structural difference between the two samples. Several notable features are observed: an overall increase in background intensity (i.e., monotonic diffuse scattering), additional broad streaks around

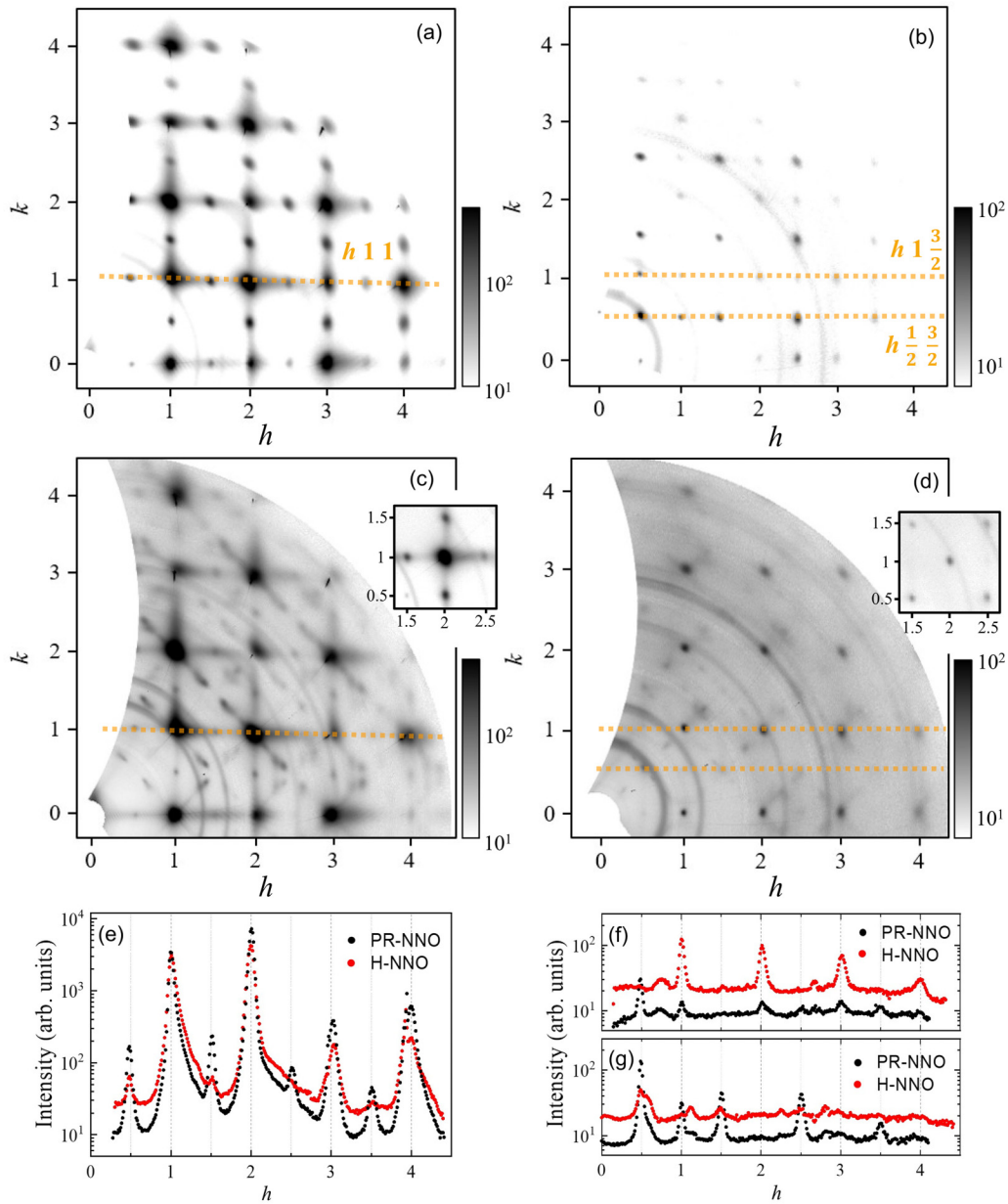


FIG. 1. Reciprocal space maps of (a) PR-NNO $hk1$, (b) PR-NNO $hk\frac{3}{2}$, (c) H-NNO $hk1$, and (d) H-NNO $hk\frac{3}{2}$, together with line profiles along (e) the $h11$, (f) the $hk\frac{3}{2}$, and (g) the $h11$ lines. The intensity is shown on a logarithmic scale in all panels. The insets in (c) and (d) display the maps after removing hydrogen from H-NNO.

integer h , k , and l positions along diagonal directions, and significant changes in the intensities of weak Bragg reflections at half-integer positions. The increased diffuse scattering suggests enhanced structural disorder. The additional diagonal streaks indicate that hydrogen doping induces an incommensurate transverse-mode lattice modulation characterized by the wave vector of $(x, -x, 0)$ (see the Appendix for details). At $x \simeq 0.37$, these modulations manifest as superlattice peaks. The streaks extending toward the Bragg reflections are similar to the scatterings reported for $\text{Pr}_{0.5}\text{Ca}_{0.5}\text{MnO}_3$ [40], which were regarded as a signature of short-range correlation among point defects. Changes in half-integer reflection intensities reveal changes in the long-range ordered structure. Since quantitative structure analysis of systems with incommensurate modulations is inherently difficult, we examine the

structure of H-NNO qualitatively based on the diffraction intensity distribution. The insets in Figs. 1(c) and 1(d) show the reciprocal space maps after removing the hydrogen from H-NNO. It is clear that incommensurate peaks have disappeared while the intensity distribution of $(\frac{1}{2}, 0, 0)$ and $(0, 0, \frac{1}{2})$ reflections has modified. This implies that the structural change by hydrogen doping is reversible, except for a domain repopulation.

Line profiles along the yellow horizontal lines in Figs. 1(a)–1(d) are presented in Figs. 1(e)–1(g). Panel (e) shows the profiles along the $h11$ line. The intensities of strong peaks at $h = 1$ and 2 for the two samples are nearly the same. In general, strong Bragg intensities are dominated by overall structural features and are insensitive to the details of structural modulation; therefore, this similarity indicates

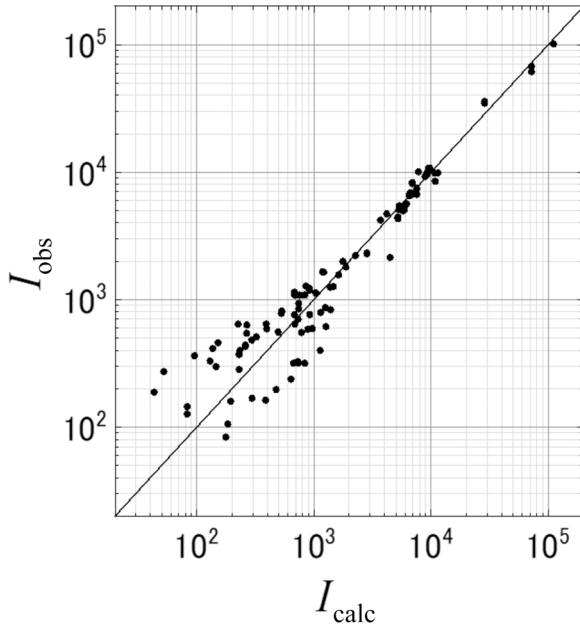


FIG. 2. Observed intensity I_{obs} vs calculated intensity I_{calc} based on the resulting structure model of the PR-NNO film.

that the illumination conditions for the two measurements were similar. In the high- h region ($h = 3$ and 4), the intensity for H-NNO is weaker than that for PR-NNO, possibly due to larger atomic displacement parameters (U 's) in H-NNO. Importantly, H-NNO shows negligible intensity at positions characterized by the wave vector $(\frac{1}{2}, 0, 0)$. This reduction indicates suppression of the PR-NNO structural modulation characterized by $(001)_o$, which involves A-site displacements, in domains with $c_o \parallel a_{pc}$.

Profiles along the $(h\frac{1}{2}\frac{3}{2})$ line shown in panel (g) exhibit substantial reduction in the intensities of peaks characterized by the wave vector $(\frac{1}{2}, \frac{1}{2}, \frac{1}{2})$ in H-NNO. The intensity of these reflections is a measure of NiO_6 octahedral tilting [37,41,42]; see Appendix B for details. Therefore, H-NNO exhibits reduced alternating octahedral tilting compared to PR-NNO, and can be regarded as $1 \times 1 \times 2$ structure.

Profiles along the $(h1\frac{3}{2})$ line shown in panel (f) exhibit a pronounced increase in the intensities of peaks characterized by the wave vector $(0, 0, \frac{1}{2})$ in H-NNO. This indicates that hydrogenation induces a distinct twofold periodic order along the out-of-plane direction. The contrast in intensity with peaks at $(\frac{1}{2}, 0, 0)$ exhibits the orientational alignment of the H-NNO lattice.

IV. DISCUSSION

Our structural investigation reveals that hydrogen doping into NdNiO_3 films induces substantial structural modulation beyond simple lattice expansion. This finding has important implications for computational studies: calculations of electronic and protonic behavior in highly doped states must include detailed structural relaxation. Calculations without such relaxation, which have been performed in some previous studies, are justified only for lightly doped regimes.

While the structure of PR-NNO is essentially identical to that of bulk NdNiO_3 , Fig. 3(a), hydrogen doping produces two key structural changes: suppressed NiO_6 octahedral tilting and the emergence of an incommensurate lattice modulation. Figures 3(b) and 3(c) show transverse-mode and longitudinal-mode modulation forming a $1 \times 1 \times 2$ superstructure. The longitudinal-mode modulation involves a layered arrangement of NiO_6 octahedra having alternating volumes, suggesting layered valence ordering.

Recent scanning transmission electron microscopy (STEM) studies [29] reported that fully strained $\text{H}_x\text{-NdNiO}_3$ grown on LaAlO_3 exhibits enhanced NiO_6 tilting, which appears to contradict our x-ray observations. However, several differences exist between the two studies. First, our samples are strain-relaxed NdNiO_3 films grown on SrTiO_3 , whereas the STEM study examined strained films on LaAlO_3 . Second, diffraction and STEM probe different aspects of structure: x-ray diffraction is sensitive to long-range order, while STEM images projected atomic positions and can detect local structures even when long-range order is absent. Therefore, our observation of weak $(\frac{1}{2}, \frac{1}{2}, \frac{1}{2})$ reflections does not exclude the presence of finite octahedral tilting with substantial spatial disorder as described in Appendix B. Quantitative

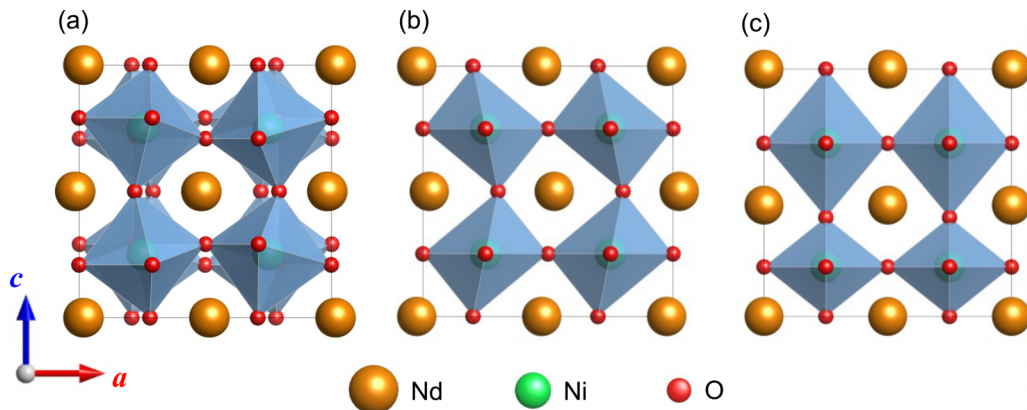


FIG. 3. (a) Structure of PR-NNO. Schematic illustrations of possible H-NNO structure with (b) longitudinal and (c) transverse displacements. All structures are viewed along the b_{pc} axis.

high-resolution structure analysis on homogeneous H-NNO samples is needed to fully resolve this discrepancy.

We now compare our findings with recent DFT calculations on $\text{H}_x\text{-SmNiO}_3$ [30]. The calculations predict that $x = 0.5$ exhibits alternating Ni^{2+} and Ni^{3+} layers, consistent with our observed twofold periodicity. This correspondence suggests a hydrogen concentration near $x = 0.5$ in H-NNO, although our experiment does not provide direct quantification. However, the calculations predict substantial octahedral tilting, contradicting our observation of suppressed tilting. This discrepancy highlights the need for computational work on H-NNO that explicitly assumes the $1 \times 1 \times 2$ structure with minimal tilting to clarify the hydrogen configuration and its effect on electronic states.

V. CONCLUDING REMARKS

We have examined the crystal structure of the hydrogen-induced insulating phase of NdNiO_3 using synchrotron x-ray diffraction. While the pristine film exhibits essentially the bulklike $\sqrt{2} \times \sqrt{2} \times 2$ structure, hydrogen doping drives a transition to a qualitatively different structural state: alternating octahedral tilting is suppressed, and a long-period order with $1 \times 1 \times 2$ periodicity along c_{pc} emerges alongside an incommensurate modulation with wave vector $(x, -x, 0)$, $x \simeq 0.37$. These observations point to a hydrogen-induced layered ordering of NiO_6 octahedra, distinct from the checkerboard charge order of pristine RNiO_3 .

Whether the commensurate $1 \times 1 \times 2$ order and the incommensurate modulation coexist within the same region or segregate spatially due to variations in hydrogen concentration remains an open question.

ACKNOWLEDGMENTS

This work was performed under the Cooperative Research Program of NJRC Mater. & Dev. (MEXT) and supported by a Grant-in-Aid for Scientific Research from the Japan Society for the Promotion of Science (JSPS KAKENHI, Grants No. JP22H02024 and No. JP23K23292). The synchrotron radiation experiments at the Photon Factory were carried out with the approval of the Photon Factory Program Advisory

Committee (Proposals No. 2022G016, No. 2023G527, and No. 2024G005).

DATA AVAILABILITY

The data that support the findings of this article are not publicly available upon publication because it is not technically feasible and/or the cost of preparing, depositing, and hosting the data would be prohibitive within the terms of this research project. The data are available from the authors upon reasonable request.

APPENDIX A: SCATTERING FROM TRANSVERSE-MODE LATTICE MODULATION

The scattering amplitude for a given scattering vector \mathbf{Q} , $F(\mathbf{Q})$, caused by a positional modulation $\mathbf{u}_n = \mathbf{u} \sin(\mathbf{q} \cdot \mathbf{R}_n)$, where \mathbf{R}_n , \mathbf{u}_n , \mathbf{u} , and \mathbf{q} denote the average position of the n th atom, displacement of the n th atom, the amplitude of the structural modulation, and the modulation vector, respectively, can be written as

$$\begin{aligned} F(\mathbf{Q}) &= \sum_n f_n \exp[i\mathbf{Q} \cdot (\mathbf{R}_n + \mathbf{u}_n)] \\ &\simeq \sum_n f_n \exp(i\mathbf{Q} \cdot \mathbf{R}_n) \\ &\quad + i\mathbf{Q} \cdot \mathbf{u} \sum_n f_n \exp(i\mathbf{Q} \cdot \mathbf{R}_n) \sin(\mathbf{q} \cdot \mathbf{R}_n), \quad (\text{A1}) \end{aligned}$$

where f_n denotes the atomic scattering factor of the n th atom. The first term produces the Bragg reflections, and the second term produces the superlattice reflections at $\mathbf{G} \pm \mathbf{q}$, where \mathbf{G} denotes the reciprocal lattice vector. The superlattice reflection term is proportional to $\mathbf{Q} \cdot \mathbf{u}$.

Figure 1(c) shows the region of $\mathbf{Q} = (h, k, 1)$ with $h, k > 0$, indicating that the component of \mathbf{u} along the $(1,1,0)$ direction is primarily observed. Each Bragg reflection is accompanied by incommensurate satellite reflections characterized by the wave vector $\mathbf{q} = (x, -x, 0)$ with $x \simeq 0.37$. Therefore, the observed incommensurate lattice modulation is predominantly of transverse character.

APPENDIX B: STRUCTURE FACTORS FOR $(\frac{1}{2}, \frac{1}{2}, \frac{1}{2})$ REFLECTIONS

Bragg peaks characterized by the wave vector $(\frac{1}{2}, \frac{1}{2}, \frac{1}{2})$ in pseudocubic notation correspond to $h + k$: odd and l : odd in $Pbnm$ notation. Calculated intensities for (hkl) : even-odd-odd reflections and odd-even-odd reflections as a function of structure parameters are presented.

(i) $h = \text{even}, k = \text{odd}, l = \text{odd}$:

$$\begin{aligned} I_{\text{ortho}}(hkl) &= |(-1)^{\frac{l+1}{2}} 4f_{\text{Nd}} \sin(2\pi h x_{\text{Nd}}) \cos(2\pi k y_{\text{Nd}}) e^{-\frac{1}{2}Q^2 U(\text{Nd})} \\ &\quad + (-1)^{k+\frac{l+1}{2}} 4f_{\text{O}} \sin(2\pi h x_{\text{O1}}) \cos(2\pi k y_{\text{O1}}) e^{-\frac{1}{2}Q^2 U(\text{O1})} \\ &\quad - (-1)^{\frac{h+k+1}{2}} 8f_{\text{O}} \sin(2\pi h x_{\text{O2}}) \sin(2\pi k y_{\text{O2}}) \sin(2\pi l z_{\text{O2}}) e^{-\frac{1}{2}Q^2 U(\text{O2})}|^2, \quad (\text{B1}) \end{aligned}$$

where X_α (X : x, y , or z , α : Nd, O1, or O2) denote the displacement of α from their $Pm\bar{3}m$ positions in the X directions, and Q is the scattering vector.

(ii) $h = \text{odd}, k = \text{even}, l = \text{odd}$:

$$\begin{aligned}
 I_{\text{ortho}}(hkl) = & |(-1)^{\frac{l+1}{2}} 4f_{\text{Nd}} \sin(2\pi hx_{\text{Nd}}) \cos(2\pi ky_{\text{Nd}}) e^{-\frac{1}{2}Q^2U(\text{Nd})} \\
 & + (-1)^{k+\frac{l+1}{2}} 4f_{\text{O}} \sin(2\pi hx_{\text{O1}}) \cos(2\pi ky_{\text{O1}}) e^{-\frac{1}{2}Q^2U(\text{O1})} \\
 & - (-1)^{\frac{h+k+1}{2}} 8f_{\text{O}} \cos(2\pi hx_{\text{O2}}) \cos(2\pi ky_{\text{O2}}) \sin(2\pi lz_{\text{O2}}) e^{-\frac{1}{2}Q^2U(\text{O2})}|^2.
 \end{aligned} \quad (\text{B2})$$

Based on the values of $x(\text{Nd})$ and $y(\text{Nd})$ in Table I, $|x_{\text{Nd}}| \simeq \frac{1}{2} |[0.5 - x(\text{Nd}) \sin 45^\circ] + [0.5 - y(\text{Nd}) \cos 45^\circ]| = 0.0012$ for PR sample, thus the f_{Nd} term can be neglected. In order to reduce the intensities of all these reflections, either (i) x_{O1} and z_{O2} are small or (ii) $U(\text{O})$ is large. If we assume that the average oxygen sites in H-NNO are the same as those in PR-NNO, $U(\text{O})$ has to be larger than 0.4 \AA^2 , which is ten times larger than PR-NNO and 100 times larger than bulk NNO. Such a large U value is physically unreasonable in well-ordered crystal lattice. Therefore, the observed reduction in $(\frac{1}{2} \frac{1}{2} \frac{1}{2})$ reflection intensity shows the suppression of alternating octahedral tilting.

-
- [1] H. Shimotani, H. Asanuma, A. Tsukazaki, A. Ohtomo, M. Kawasaki, and Y. Iwasa, Insulator-to-metal transition in ZnO by electric double layer gating, *Appl. Phys. Lett.* **91**, 082106 (2007).
- [2] K. Ueno, S. Nakamura, H. Shimotani, A. Ohtomo, N. Kimura, T. Nojima, H. Aoki, Y. Iwasa, and M. Kawasaki, Electric-field-induced superconductivity in an insulator, *Nat. Mater.* **7**, 855 (2008).
- [3] R. Scherwitzl, P. Zubko, I. G. Lezama, S. Ono, A. F. Morpurgo, G. Catalan, and J.-M. Triscone, Electric-field control of the metal-insulator transition in ultrathin NdNiO₃ films, *Adv. Mater.* **22**, 5517 (2010).
- [4] Y. Yamada, K. Ueno, T. Fukumura, H. Yuan, H. Shimotani, Y. Iwasa, L. Gu, S. Tsukimoto, Y. Ikuhara, and M. Kawasaki, Electrically induced ferromagnetism at room temperature in cobalt-doped titanium dioxide, *Science* **332**, 1065 (2011).
- [5] J. Shi, Y. Zhou, and S. Ramanathan, Colossal resistance switching and band gap modulation in a perovskite nickelate by electron doping, *Nat. Commun.* **5**, 4860 (2014).
- [6] P. Yoo and P. Liao, Metal-to-insulator transition in SmNiO₃ induced by chemical doping: A first principles study, *Mol. Syst. Des. Eng.* **3**, 264 (2018).
- [7] J. K. Wenderott, T. Billo, and D. D. Fong, Epitaxial oxide ionotronics: Interfaces and oxygen vacancies, *APL Mater.* **12**, 050901 (2024).
- [8] C. G. Van de Walle, Hydrogen as a cause of doping in zinc oxide, *Phys. Rev. Lett.* **85**, 1012 (2000).
- [9] D. M. Hofmann, A. Hofstaetter, F. Leiter, H. Zhou, F. Henecker, B. K. Meyer, S. B. Orlinskii, J. Schmidt, and P. G. Baranov, Hydrogen: A relevant shallow donor in zinc oxide, *Phys. Rev. Lett.* **88**, 045504 (2002).
- [10] H. Yoon, M. Choi, T.-W. Lim, H. Kwon, K. Ihm, J. K. Kim, S.-Y. Choi, and J. Son, Reversible phase modulation and hydrogen storage in multivalent VO₂ epitaxial thin films, *Nat. Mater.* **15**, 1113 (2016).
- [11] Y. Zhou, X. Guan, H. Zhou, K. Ramadoss, S. Adam, H. Liu, S. Lee, J. Shi, M. Tsuchiya, D. D. Fong, and S. Ramanathan, Strongly correlated perovskite fuel cells, *Nature (London)* **534**, 231 (2016).
- [12] *Localized to Itinerant Electronic Transition in Perovskite Oxides*, edited by J. B. Goodenough (Springer, Berlin, Heidelberg, New York, 2001).
- [13] J. Alonso, M. Martínez-Lope, M. Casais, J. García-Muñoz, M. Fernández-Díaz, and M. Aranda, High-temperature structural evolution of RNiO₃ ($R = \text{Ho, Y, Er, Lu}$) perovskites: Charge disproportionation and electronic localization, *Phys. Rev. B* **64**, 094102 (2001).
- [14] V. Scagnoli, U. Staub, M. Janousch, A. Mulders, M. Shi, G. Meijer, S. Rosenkranz, S. Wilkins, L. Paolasini, J. Karpinski, S. Kazakov, and S. Lovesey, Charge disproportionation and search for orbital ordering in NdNiO₃ by use of resonant x-ray diffraction, *Phys. Rev. B* **72**, 155111 (2005).
- [15] F. Serrano-Sánchez, F. Fauth, J. L. Martínez, and J. A. Alonso, Experimental observation of monoclinic distortion in the insulating regime of SmNiO₃ by synchrotron X-ray diffraction, *Inorg. Chem.* **58**, 11828 (2019).
- [16] J. Chen, Y. Zhou, S. Middey, J. Jiang, N. Chen, L. Chen, X. Shi, M. Döbeli, J. Shi, J. Chakhalian, and S. Ramanathan, Self-limited kinetics of electron doping in correlated oxides, *Appl. Phys. Lett.* **107**, 031905 (2015).
- [17] C. Oh, S. Heo, H. M. Jang, and J. Son, Correlated memory resistor in epitaxial NdNiO₃ heterostructures with asymmetrical proton concentration, *Appl. Phys. Lett.* **108**, 122106 (2016).
- [18] R. Waser and M. Aono, Nanoionics-based resistive switching memories, *Nat. Mater.* **6**, 833 (2007).
- [19] S. D. Ha, G. H. Aydogdu, and S. Ramanathan, Metal-insulator transition and electrically driven memristive characteristics of SmNiO₃ thin films, *Appl. Phys. Lett.* **98**, 012105 (2011).
- [20] R. Schmitt, J. Spring, R. Korobko, and J. L. Rupp, Design of oxygen vacancy configuration for memristive systems, *ACS Nano* **11**, 8881 (2017).
- [21] H. Liu, Y. Dong, M. Galib, Z. Cai, L. Stan, L. Zhang, A. Suwardi, J. Wu, J. Cao, C. K. I. Tan, S. K. R. S. Sankaranarayanan, B. Narayanan, H. Zhou, and D. D. Fong, Controlled formation of conduction channels in memristive devices observed by x-ray multimodal imaging, *Adv. Mater.* **34**, 2203209 (2022).
- [22] J. Chen, W. Mao, B. Ge, J. Wang, X. Ke, V. Wang, Y. Wang, M. Döbeli, W. Geng, H. Matsuzaki, J. Shi, and Y. Jiang, Revealing the role of lattice distortions in the hydrogen-induced metal-insulator transition of SmNiO₃, *Nat. Commun.* **10**, 694 (2019).
- [23] J. Chen, W. Mao, L. Gao, F. Yan, T. Yajima, N. Chen, Z. Chen, H. Dong, B. Ge, P. Zhang, X. Cao, M. Wilde, Y. Jiang, T. Terai,

- and J. Shi, Electron-doping mottronics in strongly correlated perovskite, *Adv. Mater.* **32**, 1905060 (2020).
- [24] U. Sidik, A. N. Hattori, K. Hattori, M. Alaydrus, I. Hamada, L. N. Pamasi, and H. Tanaka, Tunable proton diffusion in NdNiO₃ thin films under regulated lattice strains, *ACS Appl. Electron. Mater.* **4**, 4849 (2022).
- [25] I. Matsuzawa, T. Ozawa, Y. Nishiya, U. Sidik, A. N. Hattori, H. Tanaka, and K. Fukutani, Controlling dual Mott states by hydrogen doping to perovskite rare-earth nickelates, *Phys. Rev. Mater.* **7**, 085003 (2023).
- [26] Y. Taniguchi, H.-B. Li, A. N. Hattori, and H. Tanaka, Comprehensive determination of proton diffusion in protonated NdNiO₃ thin film by a combination of electrochemical impedance spectroscopy and optical observation, *Appl. Phys. Express* **16**, 035501 (2023).
- [27] U. Sidik, A. N. Hattori, H.-B. Li, S. Nonaka, A. I. Osaka, and H. Tanaka, Strain effect on proton-memristive NdNiO₃ thin film devices, *Appl. Phys. Express* **16**, 014001 (2023).
- [28] M. Kotiuga and K. M. Rabe, High-density electron doping of SmNiO₃ from first principles, *Phys. Rev. Mater.* **3**, 115002 (2019).
- [29] L. Gao, H. Wang, F. Meng, H. Peng, X. Lyu, M. Zhu, Y. Wang, C. Lu, J. Liu, T. Lin, A. Ji, Q. Zhang, L. Gu, P. Yu, S. Meng, Z. Cao, and N. Lu, Unveiling strong ion-electron-lattice coupling and electronic antidoping in hydrogenated perovskite nickelate, *Adv. Mater.* **35**, 2300617 (2023).
- [30] K. Yamauchi and I. Hamada, Hydrogen-induced insulating state accompanied by interlayer charge ordering in SmNiO₃, *Phys. Rev. B* **108**, 045108 (2023).
- [31] H.-B. Li, Z. Bian, M. Yoshimura, K. Shimoyama, C. Zhong, K. Shimoda, A. N. Hattori, K. Yamauchi, I. Hamada, H. Ohta, and H. Tanaka, Wide-range thermal conductivity modulation based on protonated nickelate perovskite oxides, *Appl. Phys. Lett.* **124**, 191901 (2024).
- [32] Y. Yuan, M. Kotiuga, T. J. Park, R. K. Patel, Y. Ni, A. Saha, H. Zhou, J. T. Sadowski, A. Al-Mahboob, H. Yu, K. Du, M. Zhu, S. Deng, R. S. Bisht, X. Lyu, C.-T. M. Wu, P. D. Ye, A. Sengupta, S.-W. Cheong, X. Xu, *et al.*, Hydrogen-induced tunable remanent polarization in a perovskite nickelate, *Nat. Commun.* **15**, 4717 (2024).
- [33] M. Medarde, M. T. Fernández-Díaz, and P. Lacorre, Long-range charge order in the low-temperature insulating phase of PrNiO₃, *Phys. Rev. B* **78**, 212101 (2008).
- [34] M. T. Fernández-Díaz, J. Alonso, M. Martínez-Lope, M. Casais, J. García-Muñoz, and M. Aranda, Charge disproportionation in RNiO₃ perovskites, *Physica B* **276-278**, 218 (2000).
- [35] J. L. García-Muñoz, J. Rodríguez-Carvajal, P. Lacorre, and J. Turrance, Neutron-diffraction study of RNiO₃ ($R = \text{La, Pr, Nd, Sm}$): Electronically induced structural changes across the metal-insulator transition, *Phys. Rev. B* **46**, 4414 (1992).
- [36] E. Matsubar and J.B. Cohen, The G.P. zones in Al Cu alloys—I, *Acta Metall.* **33**, 1945 (1985).
- [37] F. Izumisawa, Y. Ishii, M. Kimura, T. Katase, T. Kamiya, J.-I. Yamaura, and Y. Wakabayashi, Symmetry change in LaNiO₃ films caused by epitaxial strain from LaAlO₃, SrTiO₃, and DyScO₃ pseudocubic (001) surfaces, *J. Appl. Phys.* **136**, 075303 (2024).
- [38] M. Anada, Y. Nakanishi-Ohno, M. Okada, T. Kimura, and Y. Wakabayashi, Bayesian inference of metal oxide ultrathin film structure based on crystal truncation rod measurements, *J. Appl. Crystallogr.* **50**, 1611 (2017).
- [39] K. Nagai, M. Anada, Y. Nakanishi-Ohno, M. Okada, and Y. Wakabayashi, Robust surface structure analysis with reliable uncertainty estimation using the exchange Monte Carlo method, *J. Appl. Crystallogr.* **53**, 387 (2020).
- [40] S. Shimomura, T. Tonegawa, K. Tajima, N. Wakabayashi, N. Ikeda, T. Shobu, Y. Noda, Y. Tomioka, and Y. Tokura, X-ray diffuse scattering study on charge-localized states of Pr_{1-x}Ca_xMnO₃ ($x = 0.35, 0.4, 0.5$), *Phys. Rev. B* **62**, 3875 (2000).
- [41] Y. Wakabayashi, H. Sawa, M. Nakamura, M. Izumi, and K. Miyano, Lack of influence of anisotropic electron clouds on resonant x-ray scattering from manganite thin films, *Phys. Rev. B* **69**, 144414 (2004).
- [42] T. Fister, H. Zhou, Z. Luo, S. Seo, S. Hruszkewycz, D. Proffitt, J. Eastman, P. Fuoss, P. Baldo, H. Lee, and D. Fong, Octahedral rotations in strained LaAlO₃/SrTiO₃ (001) heterostructures, *APL Mater.* **2**, 021102 (2014).